

1 **Tropopause Evolution in a Rapidly Intensifying Tropical Cyclone: A Static**  
2 **Stability Budget Analysis in an Idealized, Axisymmetric Framework**

3 Patrick Duran\* and John Molinari

4 *University at Albany, State University of New York, Albany, NY*

5 \**Corresponding author address:* Department of Atmospheric and Environmental Sciences, Univer-  
6 sity at Albany, State University of New York, 1400 Washington Avenue, Albany, NY.

7 E-mail: pduran2008@gmail.com

## ABSTRACT

8 Large changes in tropopause-layer static stability are observed during the  
9 rapid intensification (RI) of an idealized, axisymmetric tropical cyclone (TC).  
10 Over the eye, static stability near the tropopause decreases and the cold-point  
11 tropopause height rises by up to 4 km at the storm center. Outside of the eye,  
12 static stability increases considerably just above the cold-point tropopause,  
13 and the tropopause remains near its initial level.

14 A budget analysis reveals that advection contributes to the static stability  
15 tendencies at all times throughout the upper troposphere and lower strato-  
16 sphere. Advection is particularly important within the eye, where it acts to  
17 destabilize the layer near and above the cold-point tropopause. Outside of  
18 the eye, a radial-vertical circulation develops during RI, with strong outflow  
19 below the tropopause and weak inflow above. Vertical wind shear above and  
20 below the upper-tropospheric outflow maximum induces turbulence, which  
21 provides forcing for both destabilization and stabilization in the tropopause  
22 layer. Meanwhile, as organized convection reaches the tropopause, radiative  
23 heating tendencies at the top of the cirrus canopy generally act to destabilize  
24 the upper troposphere and stabilize the lower stratosphere. Turbulent mixing  
25 and radiative heating combine to play an important role in the development  
26 of the strong stable layer immediately above the cold-point tropopause dur-  
27 ing RI. The results suggest that turbulence and radiation, alongside advection,  
28 play fundamental roles in the upper-level static stability evolution of TCs.

## 29 **1. Introduction**

30 After undergoing a remarkably rapid intensification (RI), Hurricane Patricia (2015) set a new  
31 record as the strongest tropical cyclone (TC) ever observed in the Western Hemisphere (Kim-  
32 berlain et al. 2016; Rogers et al. 2017). High-altitude dropsonde observations taken during the  
33 Tropical Cyclone Intensity (TCI) experiment captured this RI in unprecedented detail (Doyle et al.  
34 2017). These observations revealed dramatic changes in the structure of the cold-point tropopause  
35 and upper-level static stability as the storm intensified (Duran and Molinari 2018).

36 At tropical storm intensity, shortly before RI commenced, a strong inversion layer existed just  
37 above Patricia’s cold-point tropopause, which was located near 17.2 km. During the first half of  
38 the RI period, this inversion layer weakened throughout Patricia’s inner core, with the weakening  
39 most pronounced over the developing eye. By the time the storm reached its maximum intensity,  
40 the inversion layer over the eye had disappeared almost completely, which was accompanied by an  
41 increase in the tropopause height to a level at or above the highest-available dropsonde data point  
42 (18.3 km) at two locations. Meanwhile over the eyewall region, the static stability re-strengthened  
43 and the tropopause was limited to a level at or below 17.5 km. The mechanisms that led to these  
44 changes in upper-level static stability and tropopause height are the subject of the current paper.

45 Despite the importance of tropopause-layer thermodynamics in theoretical models of hurricanes  
46 (Emanuel and Rotunno 2011; Emanuel 2012), few papers have examined the upper-tropospheric  
47 evolution of TCs. Komaromi and Doyle (2017) found that stronger TCs tended to have a higher  
48 and warmer tropopause over their inner core than weaker TCs. Their results are consistent with  
49 the evolution observed over the inner core of Hurricane Patricia, in which the tropopause height  
50 increased and the tropopause temperature warmed throughout RI (Duran and Molinari 2018).

51 Idealized simulations of a TC analyzed by Ohno and Satoh (2015) suggested that the develop-  
52 ment of an upper-level warm core near the TC storm center acted to decrease the static stability  
53 near the tropopause (compare their Figs. 9,10). Although the mechanisms that drive this static  
54 stability evolution have not been examined explicitly, Stern and Zhang (2013) described the devel-  
55 opment of the TC warm core using a potential temperature ( $\theta$ ) budget analysis. They found that  
56 radial and vertical advection both played important roles in warm core development throughout  
57 RI, and subgrid-scale diffusion became particularly important during the later stage of RI. To our  
58 knowledge, the only paper that has examined explicitly the static stability evolution in a modeled  
59 TC is Kepert et al. (2016), but their analysis was limited to the boundary layer. The analysis herein  
60 is based upon that of Stern and Zhang (2013), except using a static stability budget similar to that  
61 of Kepert et al. (2016), with a focus on the upper troposphere and lower stratosphere.

## 62 **2. Model Setup**

63 The numerical simulations were performed using version 19.4 of Cloud Model 1 (CM1) de-  
64 scribed in Bryan and Rotunno (2009). The equations of motion were integrated on a 3000-km-  
65 wide, 30-km-deep axisymmetric grid with 1-km horizontal and 250-m vertical grid spacing. The  
66 computations were performed on an  $f$ -plane at 15°N latitude, over a sea surface with constant  
67 temperature of 30.5°C, which matches that observed near Hurricane Patricia (2015; Kimberlain  
68 et al. 2016). Horizontal turbulence was parameterized using the Smagorinsky scheme described in  
69 Bryan and Rotunno (2009, pg. 1773), with a prescribed mixing length that varied linearly from 100  
70 m at a surface pressure of 1015 hPa to 1000 m at a surface pressure of 900 hPa. This formulation  
71 allows for realistically-large horizontal mixing lengths near the hurricane’s inner core, consistent  
72 with the results of Bryan (2012), while not over-representing horizontal turbulence in convection  
73 at outer radii. Vertical turbulence was parameterized using the formulation of Markowski and

74 Bryan (2016, their Eq. 6), using an asymptotic vertical mixing length of 100 m and a vertically  
75 implicit Crank-Nicholson scheme. A Rayleigh damping layer was applied outside of the 2900-  
76 km radius and above the 25-km level to prevent spurious gravity wave reflection at the model  
77 boundaries. Microphysical processes were parameterized using the Thompson et al. (2004) mi-  
78 crophysics scheme and radiative heating tendencies were computed every two minutes using the  
79 Rapid Radiative Transfer Model for GCMs (RRTMG) longwave and shortwave schemes (Iacono  
80 et al. 2008). The initial temperature and humidity field was horizontally homogeneous and deter-  
81 mined by averaging all Climate Forecast System Reanalysis (CFSR) grid points within 100 km of  
82 Patricia's center of circulation at 18 UTC 21 October 2015. The vortex described in Rotunno and  
83 Emanuel (1987, their Eq. 37) was used to initialize the wind field, setting all parameters equal to  
84 the values used therein.

85 Although hurricanes simulated in an axisymmetric framework tend to be more intense than  
86 those observed in nature, the intensity evolution of this simulation matches reasonably well with  
87 that observed in Hurricane Patricia. After an initial spin-up period of about 20 hours, the modeled  
88 storm (Fig.1, blue lines) began an RI period that lasted approximately 30 hours. After this RI, the  
89 storm continued to intensify more slowly until the maximum 10-m wind speed reached  $89 \text{ m s}^{-1}$   
90 and the minimum sea-level pressure reached its minimum of 846 mb, 81 hours into the simulation.  
91 Hurricane Patricia (red stars) exhibited a similar intensity evolution, with an RI period leading to a  
92 maximum 10-m wind speed of  $95 \text{ m s}^{-1}$  and a minimum sea-level pressure of 872 hPa. Despite the  
93 limitations of the axisymmetric framework, the extraordinary intensity of Hurricane Patricia and  
94 the rapidity of its intensification makes Patricia a particularly good candidate for axisymmetric  
95 analysis.

### 96 3. Budget Computation

97 The static stability can be expressed as the squared Brunt Väisälä frequency:

$$N_m^2 = \frac{g}{T} \left( \frac{\partial T}{\partial z} + \Gamma_m \right) \left( 1 + \frac{T}{R_d/R_v + q_s} \frac{\partial q_s}{\partial T} \right) - \frac{g}{1 + q_t} \frac{\partial q_t}{\partial z}, \quad (1)$$

98 where  $g$  is gravitational acceleration,  $T$  is temperature,  $R_d$  and  $R_v$  are the gas constants of dry air  
 99 and water vapor, respectively,  $q_s$  is the saturation mixing ratio,  $q_t$  is the total condensate mixing  
 100 ratio, and  $\Gamma_m$  is the moist-adiabatic lapse rate:

$$\Gamma_m = g(1 + q_t) \left( \frac{1 + L_v q_s / R_d T}{c_{pm} + L_v \partial q_s / \partial T} \right), \quad (2)$$

101 where  $L_v$  is the latent heat of vaporization and  $c_{pm}$  is the specific heat of moist air at constant  
 102 pressure. In the tropopause layer,  $q_s$ ,  $\partial q_s / \partial T$ , and  $\partial q_t / \partial z$  approach zero. In this limiting case,  
 103 Eq. 1 reduces to:

$$N^2 = \frac{g}{\theta} \frac{\partial \theta}{\partial z}, \quad (3)$$

104 where  $\theta$  is the potential temperature.

105 To compute  $N^2$ , CM1 uses Eq.1 in saturated environments and Eq. 3 in sub-saturated environ-  
 106 ments. For simplicity, however, only Eq. 3 will be employed for the budget computations herein<sup>1</sup>.

107 Taking the time derivative of Eq. 3 yields the static stability tendency:

$$\frac{\partial N^2}{\partial t} = \frac{g}{\theta} \frac{\partial}{\partial z} \frac{\partial \theta}{\partial t} - \frac{g}{\theta^2} \frac{\partial \theta}{\partial z} \frac{\partial \theta}{\partial t}, \quad (4)$$

108 where the potential temperature tendency,  $\partial \theta / \partial t$ , can be written:

$$\frac{\partial \theta}{\partial t} = HADV + VADV + HTURB + VTURB + MP + RAD + DISS \quad (5)$$

109 Each term on the right-hand side of Eq. 5 represents a  $\theta$  budget variable, each of which is out-  
 110 put directly by the model every minute. HADV and VADV are the radial and vertical advective

---

<sup>1</sup>The validity of this approximation will be substantiated later in this section.

tendencies<sup>2</sup>, HTURB and VTURB are the radial and vertical tendencies from the turbulence parameterization, MP is the tendency from the microphysics scheme, RAD is the tendency from the radiation scheme, and DISS is the tendency due to turbulent dissipation. This equation neglects Rayleigh damping, since this term is zero everywhere below 25 km, and the analysis domain does not extend to that level. Each term in Eq. 5 is substituted for  $\partial\theta/\partial t$  in Eq. 4, yielding the contribution of each budget term to the static stability tendency. These terms are summed, yielding an instantaneous "budget change" in  $N^2$  every minute. The budget changes are then averaged over 24-hour periods and compared to the total model change in  $N^2$  over that same time period, i.e.:

$$\Delta N_{budget}^2 = \frac{1}{\delta t} \sum_{t=t_0}^{t_0+\delta t} \left. \frac{\partial N^2}{\partial t} \right|_t \quad (6)$$

$$\Delta N_{model}^2 = N_{t_0+\delta t}^2 - N_{t_0}^2 \quad (7)$$

$$Residual = \Delta N_{model}^2 - \Delta N_{budget}^2 \quad (8)$$

where  $t_0$  is an initial time and  $\delta t$  is 24 hours.

Eqs. 6-8 are plotted for four consecutive 24-hour periods in Fig. 2. For this and all subsequent radial-vertical cross sections, a 1-2-1 smoother is applied once in the radial direction to eliminate  $2\Delta r$  noise that appears in some of the raw model output and calculated fields. The left column of Fig. 2 depicts the model changes (Eq. 7), the center column depicts the budget changes (Eq. 6), and the right column depicts the residuals (Eq. 8). In every 24-hour period, the budget changes are nearly identical to the model changes, which is reflected in the near-zero residuals in the right column. This indicates that the budget accurately represents the model variability, which implies that the neglect of moisture in the budget computation introduces negligible error within the analysis domain<sup>3</sup>.

---

<sup>2</sup>These terms include the tendencies due to the diffusion that is implicit in the fifth-order advection scheme.

<sup>3</sup>This is not the case in the lower- and mid-troposphere, where the residual actually exceeds the budget variability in many places, likely due to the neglect of moisture; thus we limit this analysis to the upper troposphere and lower stratosphere.

131 In the tropopause layer, some of the budget terms are small enough to be ignored. To deter-  
 132 mine which of the budget terms are most important, a time series of the contribution of each of  
 133 the budget terms in Eq. 5 to the tropopause-layer static stability tendency is plotted in Fig. 4.  
 134 For this figure, each of the budget terms is computed using the method described in Section 3,  
 135 except with 1-hour averaging intervals instead of 24-hour intervals. The absolute values of these  
 136 tendencies are then averaged over a radius-height domain surrounding the tropopause and plotted  
 137 as a time series<sup>4</sup>. Advection (Fig. 4, red line) plays an important role in the mean tropopause-  
 138 layer static stability tendency at all times, and vertical turbulence (Fig. 4, blue line) and radiation  
 139 (Fig. 4, dark green line) also contribute significantly. Although the contribution from horizontal  
 140 turbulence (Fig. 4, purple line) becomes more important after 48 hours, it is confined to a very  
 141 small region immediately surrounding the eyewall tangential velocity maximum (not shown), and  
 142 is negligible throughout the rest of the tropopause layer. The remaining two processes - micro-  
 143 physics and dissipative heating (Fig. 4, orange and light green lines, respectively) - lie atop one  
 144 another near zero. Although the latent heating term can be quite large in the eyewall region, it is  
 145 negligible everywhere outside of the eyewall, as are the effects of dissipative heating. These time  
 146 series indicate that, at all times, three budget terms dominate the tropopause-layer static stability  
 147 tendency: advection, vertical turbulence, and radiation. Variations in the magnitude and spatial  
 148 structure of these terms drive the static stability changes depicted in Fig. 2; subsequent sections  
 149 will focus on these variations and what causes them.

---

<sup>4</sup>It will be seen in subsequent figures that each of the terms contributes both positively and negatively to the  $N^2$  tendency within the analysis domain. Thus, taking an average over the domain tends to wash out the positive and negative contributions. To circumvent this problem, the absolute value of each of the terms is averaged.



## 4. Results

### *a. Static stability evolution*

The average  $N^2$  over the first day of the simulation (Fig. 3a) indicates the presence of a weak static stability maximum just above the cold-point tropopause. Over the subsequent 24 hours, during the RI period, the static stability within and above this layer decreased near the storm center (Fig. 3b). This decreasing  $N^2$  corresponded to an increase in the tropopause height within the developing eye, maximized at the storm center. Outside of the eye, meanwhile, the tropopause height decreased over the eyewall region (25-60-km radius) and increased only slightly outside of the 60-km radius. In this outer region, the  $N^2$  maximum just above the tropopause strengthened during RI. These trends continued as the storm's intensity leveled off in the 48-72-hour period (Fig. 3c). The tropopause height increased to nearly 21 km at the storm center and sloped sharply downward to 16.3 km on the inner edge of the eyewall, near the 30 km radius. Static stability outside of the eye, meanwhile, continued to increase just above the cold-point tropopause. This  $N^2$  evolution closely follows that observed in Hurricane Patricia (2015; Duran and Molinari 2018). The mechanisms that led to these static stability changes will be investigated in the subsequent sections.

### *b. Static stability budget analysis*

*(i) 0-24 hours* The weakening of the lower-stratospheric static stability maximum during the initial spin-up period is reflected in the total  $N^2$  budget change over this time (Fig. 5a). The 17-18-km layer was characterized by decreasing  $N^2$  (purple shading), maximizing at the storm center. The layer immediately below the tropopause, meanwhile, saw strengthening  $N^2$  during this time period. Although these tendencies extended out to the 200-km radius, they were particularly

pronounced at innermost radii. A comparison of the contributions of advection (Fig. 5b), vertical turbulence (Fig. 5c), and radiation (Fig. 5d) reveals that advection was primarily responsible for the change in static stability during this period. Although vertical turbulence acted in opposition to advection (i.e. it acted to stabilize regions that advection acted to destabilize), the magnitude of the advective tendencies was larger, particularly at the innermost radii. The sum of advection and vertical turbulence (Fig. 5e) almost exactly replicated the static stability tendencies above 17 km. Radiative tendencies, meanwhile, (Fig. 5d) acted to destabilize the layer below about 16 km and stabilize the layer between 16 and 17 km. The sum of advection, vertical turbulence, and radiation (Fig. 5f) reproduces the total change in  $N^2$  almost exactly.

(ii) *24-48 hours* During the RI period,  $N^2$  within the eye generally decreased above 16 km and increased below (Fig. 6a). These tendencies at the innermost radii were driven almost entirely by advection (Fig. 6b); vertical turbulence (Fig. 6c) and radiation (Fig. 6d) contributed negligibly to the static stability tendencies in this region.

Outside of the eye, the  $N^2$  evolution exhibited alternating layers of positive and negative tendencies. Near and above 18 km existed an upward-sloping region of decreasing  $N^2$  that extended out to the 180-km radius. In this region, neither vertical turbulence nor radiation exhibited negative  $N^2$  tendencies; advection was the only forcing for destabilization. Immediately below this layer was a region of increasing  $N^2$ , which sloped upward from 17 km near the 30-km radius to just below 18 km outside of the 100-km radius. Advection and vertical turbulence both contributed to this positive  $N^2$  tendency, with advection playing an important role below about 17.5 km and and turbulence playing an important role above. The sum of advection and turbulence (Fig. 6e) reveals two discontinuous regions of increasing  $N^2$  in the 17-18-km layer rather than one contiguous region. The addition of radiation to these two terms, however, (Fig. 6f) provides the link between

195 these two regions, indicating that radiation also plays a role in strengthening the stable layer just  
196 above the tropopause. In the 16-17-km layer, a horizontally-extensive layer of decreasing  $N^2$  also  
197 was forced by a combination of advection, vertical turbulence, and radiation. The sum of advec-  
198 tion and vertical turbulence accounts for only a portion of the decreasing  $N^2$  in this layer, and  
199 actually indicates forcing for stabilization near the 50-km radius and outside of the 130-km radius.  
200 Radiative tendencies overcome this forcing for stabilization in both of these regions to produce the  
201 radially-extensive region of destabilization observed just below the tropopause.

202 The sum of advection, vertical turbulence, and radiation (Fig. 6f) once again closely follows the  
203 observed  $N^2$  variability, except in portions of the eyewall where the neglect of latent heating and  
204 horizontal turbulence introduces some differences.

205 (iii) 48-72 hours After the storm's maximum wind speed leveled off near  $80 \text{ m s}^{-1}$ , the magnitude  
206 of the static stability tendencies within the eye decreased to near zero (Fig. 7a).

207 Outside of the eye, however,  $N^2$  continued to increase just above the tropopause and decrease  
208 just below. The sum of advection and vertical turbulence (Fig. 7e) indicates that the increase of  
209  $N^2$  observed in the 17-18-km layer and inside of the 80-km radius cannot be attributed to these  
210 processes, since the sum of these two terms provided forcing for destabilization. Instead, radiation  
211 (Fig. 7d), provided the forcing for stabilization in this region. Outside of the 80-km radius, both  
212 advection (Fig. 7b) and vertical turbulence (Fig. 7c) provided forcing for stabilization near the  
213 18-km level. The sum of the two terms indicates increasing  $N^2$  near the 18-km level everywhere  
214 outside of the 80-km radius, but this stabilization is slightly weaker in the 90-120-km radial band  
215 than the observed value. The addition of radiation (Fig. 7f) provides the extra forcing for stabi-  
216 lization required to account for the observed increase in  $N^2$ . Outside of the 120-km radius, the  
217 region of radiative forcing for stabilization slopes downward, and the increase in  $N^2$  observed near

18 km can be explained entirely by a combination of advection and vertical turbulence. The layer of decreasing  $N^2$  observed near 17 km was forced primarily by vertical turbulence and radiation. Within most of this region, advection provided strong forcing for stabilization, but this forcing was outweighed by the negative  $N^2$  tendencies induced by a combination of vertical turbulence and radiation.

## 5. Discussion

### *a. The role of advection*

Advection played an important role in the tropopause-layer  $N^2$  evolution at all stages of intensification, but for brevity, this section will focus only on the RI (24-48-hour) period. To investigate the advective processes more closely, the individual contributions of horizontal and vertical advection during the RI period are shown in Fig. 8, along with the corresponding time-mean radial and vertical velocities and  $\theta$ . The  $N^2$  tendencies due to the two advective components (Fig. 8a,b) exhibit strong cancellation, consistent with flow that is nearly isentropic. There are, however, many regions in which flow crosses  $\theta$  surfaces; this flow accounts for all non-zero  $N^2$  tendencies due to advection previously seen in Fig. 6b.

Some insight can be gained by considering the time tendency of the vertical  $\theta$  gradient due to advection:

$$\left( \frac{\partial}{\partial t} \frac{\partial \theta}{\partial z} \right)_{adv} = -u \frac{\partial}{\partial r} \frac{\partial \theta}{\partial z} - w \frac{\partial}{\partial z} \frac{\partial \theta}{\partial z} - \frac{\partial u}{\partial z} \frac{\partial \theta}{\partial r} - \frac{\partial w}{\partial z} \frac{\partial \theta}{\partial z}. \quad (9)$$

The first two terms on the right-hand side of Eq. 9 represent advection of static stability by the radial and vertical wind, respectively. These terms cannot create a maximum or a minimum; they only act to rearrange the static stability field. The third and fourth terms represent, respectively, the tilting of isentropes in the presence of vertical wind shear, and the spreading or compaction

239 of isentropes through divergence of the vertical wind. Since these terms involve gradients of  
 240 velocities, they can create or eliminate local maxima or minima in static stability.

241 During the RI period, strong radial and vertical circulations developed near the tropopause,  
 242 which forced high-magnitude  $N^2$  tendencies due to advection (Fig. 8a,b). A layer of strong outflow  
 243 developed at and below the tropopause during this period, with the outflow maximum (dashed cyan  
 244 line) curving from the 14-km level at the 50-km radius to just below the 16-km level outside of  
 245 the 80-km radius (Fig. 8c). The cyan line, by definition, represents the level at which the vertical  
 246 gradient of radial velocity switched signs, with  $\partial u / \partial z > 0$  below the line and  $\partial u / \partial z < 0$  above.  
 247 Notably, the  $N^2$  tendency due to horizontal advection (Fig. 8a) also tended to switch signs at this  
 248 line, with stabilization below the outflow maximum and destabilization above. Examination of  
 249 the third term on the right-hand side of Eq. 9 suggests that tilting of isentropes within these shear  
 250 layers contributed to the strong  $N^2$  tendencies that flanked the outflow maximum. Outside of the  
 251 eye and eyewall, isentropes generally sloped upward with radius, which means that  $\theta$  decreased  
 252 outward ( $\partial \theta / \partial r < 0$ ). Thus, wherever  $\partial u / \partial z > 0$ , the tilting term must force an increase in  $N^2$ ,  
 253 and wherever  $\partial u / \partial z < 0$ , the tilting term must force a decrease in  $N^2$ , which is precisely the  
 254 structure seen in Fig. 8a.

255 Advection of  $N^2$  by the radial wind (first term on the right-hand side of Eq. 9) also acted  
 256 within the outflow jet. For example, horizontal advection provided forcing for destabilization at  
 257 the 16-km level almost everywhere inside of the 140-km radius. Outside of this radius near 16 km,  
 258 however, existed a region of forcing for stabilization. This switch in signs was a consequence of a  
 259 reversal of the radial gradient of mean  $N^2$  near the 140-km radius (Fig. 3b). Inside of that radius,  
 260  $(\partial / \partial r)(\partial \theta / \partial z) > 0$  and  $u > 0$ , which corresponds to forcing for destabilization in Eq. 9; outside  
 261 of that radius  $(\partial / \partial r)(\partial \theta / \partial z) < 0$  and  $u > 0$ , which corresponds to forcing for stabilization.

262 The relative importance of the first and third terms on the right-hand side of Eq. 9 is difficult to  
263 ascertain, but the structure of the mean radial velocity,  $\theta$ , and  $N^2$  fields suggests that both terms  
264 are contributing within the outflow layer.

265 Meanwhile in the lower stratosphere, a thin layer of  $2\text{--}4\text{ m s}^{-1}$  inflow developed a few hundred  
266 meters above the tropopause, similar to that which was observed in Hurricane Patricia (2015;  
267 Duran and Molinari 2018) and in previous modeling studies (e.g. Ohno and Satoh 2015; Kieu  
268 et al. 2016). Since the isentropes in this layer sloped slightly upward with radius (i.e.  $\partial\theta/\partial r < 0$ ),  
269 this inflow acted to import lower  $\theta$  air from outer radii to inner radii. Decreasing  $\theta$  near the inflow  
270 maximum acted to destabilize the layer below the inflow maximum and stabilize the layer above  
271 (Fig. 8a).

272 Vertical advection also played an important role in the tropopause-layer static stability evolution.  
273 Within the eye, subsidence dominated below 17 km, while mean ascent existed near the storm  
274 center above 17 km<sup>5</sup>. Although the magnitude of the subsidence was larger at lower altitudes,  
275  $\partial\theta/\partial z$  was smaller there. Because  $\partial\theta/\partial z$  was smaller, the subsidence at lower levels could not  
276 accomplish as much warming as the subsidence at higher levels in the eye, consistent with the  
277 results of Stern and Zhang (2013).

278 Outside of the eye, ascent dominated the troposphere, while a 1.5-km-deep layer of descent  
279 existed immediately above the tropopause. This region of descent

## 280 *b. The role of radiation*

281 During the initial spin-up period (0–24 hours; 9a), convection was not deep enough to deposit  
282 large quantities of ice near the tropopause in the mean. Due to the lack of ice particles, the

---

<sup>5</sup>Close examination of the model output revealed that this mean ascent was forced by the interaction of inward-propagating waves with the boundary at  $r=0$ . When a wave reached  $r=0$ , a dipole of vertical velocity resulted, with ascent above and subsidence below. For reasons that remain unclear, the regions of ascent were more persistent than the regions of subsidence, which resulted in mean ascent near  $r=0$  in the lower stratosphere.

radiative heating tendencies during this period (Fig. 9b) were relatively small and confined to the region above a few particularly strong convective towers. During RI (24-48 hours; Fig. 9b), the eyewall updraft strengthened and a radially-extensive cirrus canopy developed near the tropopause. The enhanced vertical gradient of ice mixing ratio at the top of the cirrus canopy induced strong diurnal-mean radiative cooling near the tropopause (9d). This cooling exceeded  $0.6 \text{ K h}^{-1}$  in some places and sloped downward from the lower stratosphere into the upper troposphere, following the top of the cirrus canopy. A small radiative warming maximum also appeared outside of the 140-km radius below this region of cooling. These results broadly agree with those of Bu et al. (2014; see their Fig. 11a), whose CM1 simulations 0.3 K net diurnally-averaged radiative cooling at the top of the cirrus canopy and radiative warming within the cloud maximized near the 200-km radius. The broad region of radiative cooling acted to destabilize the layer below the cooling maximum and stabilize the layer above, which can be seen in Fig. 6d. The small area of net radiative heating outside of the 140-km radius enhanced the destabilization in this region and produced a thin layer of stabilization in the 15-16-km layer.

After the TC's RI period completed (48-72 hours; Fig. 9f), strong radiative cooling remained near the tropopause at inner radii, sloping downward with the top of the cirrus canopy to below the tropopause at outer radii. Cooling rates exceeded  $1 \text{ K h}^{-1}$  just above the tropopause between the 30- and 70-km radii. These cooling rates exceeded those observed by Bu et al. (2014), a discrepancy that is a consequence of their larger vertical grid spacing (625 m) compared to that used here (250 m), along with a contribution from differing radiation schemes<sup>6</sup>. Time-mean radiative warming spread from 30- to 160-km radius within the cirrus canopy. The existence of radiative cooling

---

<sup>6</sup>Bu et al. (2014) employed the NASA-Goddard radiation scheme for their CM1 simulations, whereas RRTMG is used in the present paper. A simulation using NASA-Goddard radiation and 625-m vertical grid spacing produced maximum radiative cooling rates of  $0.3 \text{ K h}^{-1}$ , which agrees with the rates in Bu et al. (2014). Another simulation using 625-m vertical grid spacing and RRTMG radiation produced cooling rates of up to  $0.6 \text{ K h}^{-1}$ .

304 overlying radiative warming in this region led to radiatively-forced destabilization at and below  
305 the tropopause, as was observed in Fig. 7d. Below the warming layer existed a region of forcing  
306 for stabilization, while a much stronger region of forcing for destabilization existed above the  
307 cooling maximum in the lower stratosphere.

308 The results herein suggest that radiative heating tendencies played an important role in destabi-  
309 lizing the upper troposphere and stabilizing the lower stratosphere after the cirrus canopy devel-  
310 oped and persisted during and after RI.

### 311 *c. The role of turbulent mixing*

312 Although vertical turbulence always acts to eliminate vertical gradients of  $\theta$ , this adjustment  
313 toward a neutral state only occurs where the mixing takes place. If turbulence occurs in a stably-  
314 stratified layer, it will act to decrease  $\theta$  at the top of the layer and increase it below. Just above and  
315 just below the mixed layer, however, the  $\theta$  profile remains undisturbed. Consequently, although  
316 turbulent mixing acts to decrease  $\partial\theta/\partial z$  in the layer in which it is occurring, it actually increases  
317  $\partial\theta/\partial z$  just below and just above the layer. These vertical gradients of turbulent mixing are quite  
318 important, particularly on the flanks of the upper-tropospheric outflow jet.

319 Fig. 10 reveals that two distinct maxima of vertical eddy diffusivity developed in the tropopause  
320 layer as the storm intensified. Comparison of these turbulent regions to the  $N^2$  tendencies in Figs.  
321 6c and 7c reveals that the layers in which vertical eddy diffusivity maximized corresponded to  
322 layers of destabilization due to vertical turbulence. Just outside of these layers, however, vertical  
323 turbulence acted to increase  $N^2$ . The large vertical gradient of vertical eddy diffusivity near the  
324 tropopause played an important role in developing the lower-stratospheric stable layer during RI.  
325 This supports the hypothesized role of turbulence in setting the outflow-layer  $\theta$  stratification in  
326 Rotunno and Emanuel (1987).



## 6. Conclusions

The simulated  $N^2$  evolution shown herein closely matched that observed during the RI of Hurricane Patricia (2015). Three processes dominated the  $N^2$  variability in the upper troposphere and lower stratosphere: advection, radiation, and vertical turbulence. Radiation and vertical turbulence played particularly important roles in developing the strong  $N^2$  maximum just above the cold-point tropopause during RI. Since these two processes are parameterized, and radiation closely depends on yet another parameterized process (microphysics), the tropopause-layer  $N^2$  variability could be quite sensitive to the assumptions inherent to parameterizations used. A number of sensitivity experiments revealed that the details of the  $N^2$  evolution were sensitive to the selection of the microphysics scheme, the vertical turbulence length scale, and the vertical grid spacing. All of the simulations, however, did develop an elevated tropopause over the eye that corresponded to decreasing static stability and, outside of the eye, an  $N^2$  maximum immediately above the tropopause.

Comparison to previous work revealed that small vertical grid spacing is necessary to resolve the shallow layer of radiative cooling at the top of the cirrus canopy. Increasing the vertical grid spacing decreased the magnitude of the radiative cooling and produced a weaker, but deeper lower-stratospheric stable layer.

In this paper, all of the variables were averaged over a full diurnal cycle to eliminate the effects of diurnal variability and isolate the overall storm evolution. Diurnal variations in static stability near the tropopause are potentially of interest with respect to the tropical cyclone diurnal cycle, however, and will be the subject of future work.

*Acknowledgments.* We are indebted to George Bryan for his continued development and support of Cloud Model 1. We also thank Jeffrey Kepert, Robert Fovell, and Erika Navarro for helpful conversations related to this work. This research was supported by NSF Grant #1636799.

## APPENDIX

### Sensitivity experiments

The simulations exhibited some sensitivity to the initial thermodynamic profile and the prescribed vertical mixing length. Although the details of the intensification and the tropopause-layer  $N^2$  evolution varied when these quantities were changed, the conclusions of the paper remain unchanged.

#### *a. Sensitivity to the initial thermodynamic profile*

A number of sensitivity experiments were conducted using a variety of initial soundings. Changing the initial temperature and humidity profiles affected the timing of the onset of organized deep convection and the rapidity of intensification. In all simulations, however, convection eventually penetrated to the tropopause, at which time vertical turbulence and radiation combined with advection to adjust the  $N^2$  profile toward that which was observed in the control run. By the end of the RI period in every simulation, all three processes were actively modifying the  $N^2$  profile near the tropopause.

As an example, 24-hour averages of  $N^2$  are plotted in Fig. b for a simulation that was identical to that used in this paper, except the initial sounding was determined by averaging every grid point within 1000 km of TC Patricia's storm center at 18 UTC 21 October 2015 instead of averaging only within the 100-km radius. Although the lower-stratospheric stable layer developed more slowly and was weaker than that shown in Fig. 3, the overall evolution was quite similar and the same budget terms dominated the static stability evolution (not shown).

*b. Sensitivity to the vertical mixing length*

The rate of turbulent mixing in the Smagorinsky scheme used herein is highly dependent on a prescribed length scale. The vertical mixing length used in this paper (100 m) was based on the sensitivity experiments of Bryan (2012). Prescribing a smaller mixing length produces smaller  $\theta$  tendencies due to turbulence, but even with a mixing length on the low end of those tested by Bryan (2012), turbulence still played an important role in the tropopause-layer  $N^2$  evolution. Fig. b shows the 24-hour-averaged contributions of turbulent mixing to the  $N^2$  evolution from a simulation identical to that used in this paper, except with a vertical mixing length of 50 m. At all times, vertical turbulence still played an important role in the tropopause-layer static stability evolution, particularly during the latter stages of RI (48-72 hours).

**References**

- Bryan, G. H., 2012: Effects of surface exchange coefficients and turbulence length scales on the intensity and structure of numerically simulated hurricanes. *Mon. Wea. Rev.*, **140**, 1125–1143.
- Bryan, G. H., and R. Rotunno, 2009: The maximum intensity of tropical cyclones in axisymmetric numerical model simulations. *Mon. Wea. Rev.*, **137**, 1770–1789.
- Bu, Y. P., R. G. Fovell, and K. L. Corbosiero, 2014: Influence of cloud-radiative forcing on tropical cyclone structure. *J. Atmos. Sci.*, **71**, 1644–1622.
- Doyle, J. D., and Coauthors, 2017: A view of tropical cyclones from above: The Tropical Cyclone Intensity (TCI) Experiment. *Bull. Amer. Meteor. Soc.*, **98**, 2113–2134.
- Duran, P., and J. Molinari, 2018: Dramatic inner-core tropopause variability during the rapid intensification of Hurricane Patricia (2015). *Mon. Wea. Rev.*, **146**, 119–134.

391 Emanuel, K., 2012: Self-stratification of tropical cyclone outflow. Part II: Implications for storm  
 392 intensification. *J. Atmos. Sci.*, **69**, 988–996.

393 Emanuel, K., and R. Rotunno, 2011: Self-stratification of tropical cyclone outflow. Part I: Impli-  
 394 cations for storm structure. *J. Atmos. Sci.*, **68**, 2236–2249.

395 Iacono, M. J., J. S. Delamere, E. J. Mlawer, M. W. Shephard, S. A. Clough, and W. D. Collins,  
 396 2008: Radiative forcing by long-lived greenhouse gases: Calculations with the AER radiative  
 397 transfer models. *J. Geophys. Res.*, **113** (D13103).

398 Kepert, J. D., J. Schwendike, and H. Ramsay, 2016: Why is the tropical cyclone boundary layer  
 399 not "well mixed"? *J. Atmos. Sci.*, **73**, 957–973.

400 Kieu, C., V. Tallapragada, D.-L. Zhang, and Z. Moon, 2016: On the development of double warm-  
 401 core structures in intense tropical cyclones. *J. Atmos. Sci.*, **73**, 4487–4506.

402 Kimberlain, T. B., E. S. Blake, and J. P. Cangialosi, 2016: Tropical cyclone report: Hurricane  
 403 Patricia. National Hurricane Center. [Available online at [www.nhc.noaa.gov](http://www.nhc.noaa.gov)].

404 Komaromi, W. A., and J. D. Doyle, 2017: Tropical cyclone outflow and warm core structure as  
 405 revealed by HS3 dropsonde data. *Mon. Wea. Rev.*, **145**, 1339–1359.

406 Markowski, P. M., and G. H. Bryan, 2016: LES of laminar flow in the PBL: A potential problem  
 407 for convective storm simulations. *Mon. Wea. Rev.*, **144**, 1841–1850.

408 Ohno, T., and M. Satoh, 2015: On the warm core of a tropical cyclone formed near the tropopause.  
 409 *J. Atmos. Sci.*, **72**, 551–571.

410 Rogers, R. F., S. Aberson, M. M. Bell, D. J. Cecil, J. D. Doyle, J. Morgerman, L. K. Shay, and  
 411 C. Velden, 2017: Re-writing the tropical record books: The extraordinary intensification of  
 412 Hurricane Patricia (2015). *Bull. Amer. Meteor. Soc.*, **98**, 2091–2112.

413 Rotunno, R., and K. A. Emanuel, 1987: An air-sea interaction theory for tropical cyclones. Part II:  
414 Evolutionary study using a nonhydrostatic axisymmetric numerical model. *J. Atmos. Sci.*, **44**,  
415 542–561.

416 Stern, D. P., and F. Zhang, 2013: How does the eye warm? Part I: A potential temperature budget  
417 analysis of an idealized tropical cyclone. *J. Atmos. Sci.*, **70**, 73–89.

418 Thompson, G., R. M. Rasmussen, and K. Manning, 2004: Explicit forecasts of winter precipitation  
419 using an improved bulk microphysics scheme. Part I: Description and sensitivity analysis. *Mon.*  
420 *Wea. Rev.*, **132**, 519–542.

## 421 LIST OF FIGURES

422	<b>Fig. 1.</b>	The maximum 10-m wind speed (top panel; $\text{m s}^{-1}$ ) and minimum sea-level pressure (bottom	
423		panel; hPa) in the simulated storm (blue lines) and from Hurricane Patricia's best track (red	
424		stars). . . . .	25
425	<b>Fig. 2.</b>	Left panels: Twenty-four-hour changes in squared Brunt-Väisälä frequency ( $N^2$ ; $10^{-4} \text{ s}^{-2}$ )	
426		over (top row) 0-24 hours, (middle row) 24-48 hours, (bottom row) 48-72 hours. Middle	
427		Panels: The $N^2$ change over the same time periods computed using Eqs. 4-6, Right Panels:	
428		The budget residual over the same time periods, computed by subtracting the budget change	
429		(middle column) from the model change (left column). . . . .	26
430	<b>Fig. 3.</b>	Twenty-four-hour averages of squared Brunt-Väisälä frequency ( $N^2$ ; $10^{-4} \text{ s}^{-2}$ ) over (a) 0-24	
431		hours, (b) 24-48 hours, (c) 48-72 hours. Orange lines represent the cold-point tropopause	
432		averaged over the same time periods. . . . .	27
433	<b>Fig. 4.</b>	Time series of the contribution of each of the budget terms to the time tendency of the	
434		squared Brunt-Väisälä frequency ( $N^2$ ; $10^{-4} \text{ s}^{-2}$ ). For each budget term, the absolute value	
435		of the $N^2$ tendency is averaged temporally over 1-hour periods (using output every minute),	
436		and spatially in a region extending from 0 to 200 km radius and 14 to 21 km altitude. . . . .	28
437	<b>Fig. 5.</b>	(a) Total change in $N^2$ over the 0-24-hour period ( $10^{-4} \text{ s}^{-2} (24 \text{ h})^{-1}$ ) and the contributions to	
438		that change from (b) the sum of horizontal and vertical advection, (c) vertical turbulence, (d)	
439		longwave and shortwave radiation, (e) the sum of horizontal advection, vertical advection,	
440		and vertical turbulence, and (f) the sum of horizontal advection, vertical advection, vertical	
441		turbulence, and longwave and shortwave radiation. . . . .	30

442	<b>Fig. 6.</b>	As in Fig. 5, but for the 24-48-hour period. . . . .	31
443	<b>Fig. 7.</b>	As in Fig. 5, but for the 48-72-hour period. . . . .	32
444	<b>Fig. 8.</b>	The contribution to the change in $N^2$ over the 24-48-hour period ( $10^{-4} \text{ s}^{-2} (24 \text{ h})^{-1}$ ) by (a) hor-	
445		izontal advection and (b) vertical advection. (c) The radial velocity ( $\text{m s}^{-1}$ ; filled contours),	
446		potential temperature (K; thick black contours), cold-point tropopause height (orange line),	
447		and level of maximum outflow (dashed cyan line) averaged over the 24-48-hour period. (d)	
448		The vertical velocity ( $\text{cm s}^{-1}$ ; filled contours), potential temperature (K; thick black con-	
449		tours), and cold-point tropopause height (orange line) averaged over the 24-48-hour period.	
450		33	
451	<b>Fig. 9.</b>	Ice mixing ratio ( $\text{g kg}^{-1}$ ) and cold-point tropopause height (orange lines) averaged over (a)	
452		0-24 hours, (c) 24-48 hours, and (e) 48-72 hours. Radiative heating rate ( $\text{K h}^{-1}$ ) and cold-	
453		point tropopause height (orange lines) averaged over (b) 0-24 hours, (d) 24-48 hours, and (f)	
454		48-72 hours. . . . .	35
455	<b>Fig. 10.</b>	Vertical eddy diffusivity ( $\text{m}^2 \text{ s}^{-2}$ ; filled contours), cold-point tropopause height (cyan lines),	
456		and radial velocity ( $\text{m s}^{-1}$ ; thick black lines) averaged over (a) 0-24 hours, (b) 24-48 hours,	
457		and (c) 48-72 hours. . . . .	36
458	<b>Fig. A1.</b>	Twenty-four-hour averages of squared Brunt-Väisälä frequency ( $N^2$ ; $10^{-4} \text{ s}^{-2}$ ) over (a) 0-24	
459		hours, (b) 24-48 hours, (c) 48-72 hours, and (d) 72-96 hours for the simulation described in	
460		Appendix Aa. Orange lines represent the cold-point tropopause averaged over the same time	
461		periods. . . . .	37

462 **Fig. A2.** The contribution of vertical turbulence to the  $N^2$  variability ( $10^{-4} \text{ s}^{-2} (24 \text{ h})^{-1}$ ) averaged over  
 463 (a) 0-24 hours, (b) 24-48 hours, (c) 48-72 hours, and (d) 72-96 hours for the simulation  
 464 described in Appendix Ab. . . . . 38



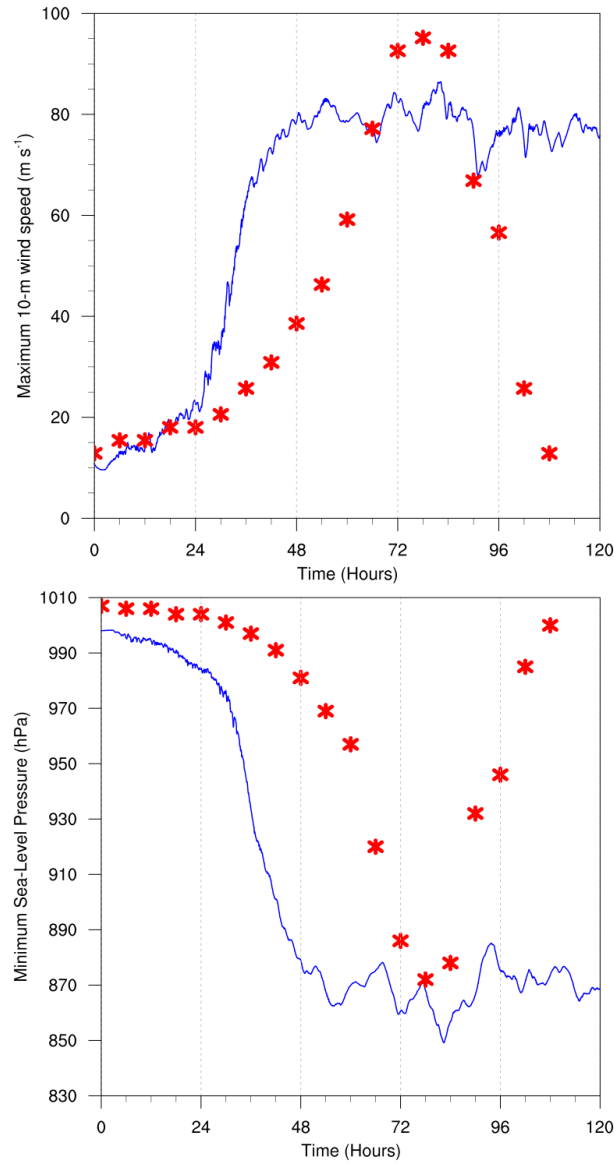


FIG. 1. The maximum 10-m wind speed (top panel; m s<sup>-1</sup>) and minimum sea-level pressure (bottom panel;  
hPa) in the simulated storm (blue lines) and from Hurricane Patricia's best track (red stars).

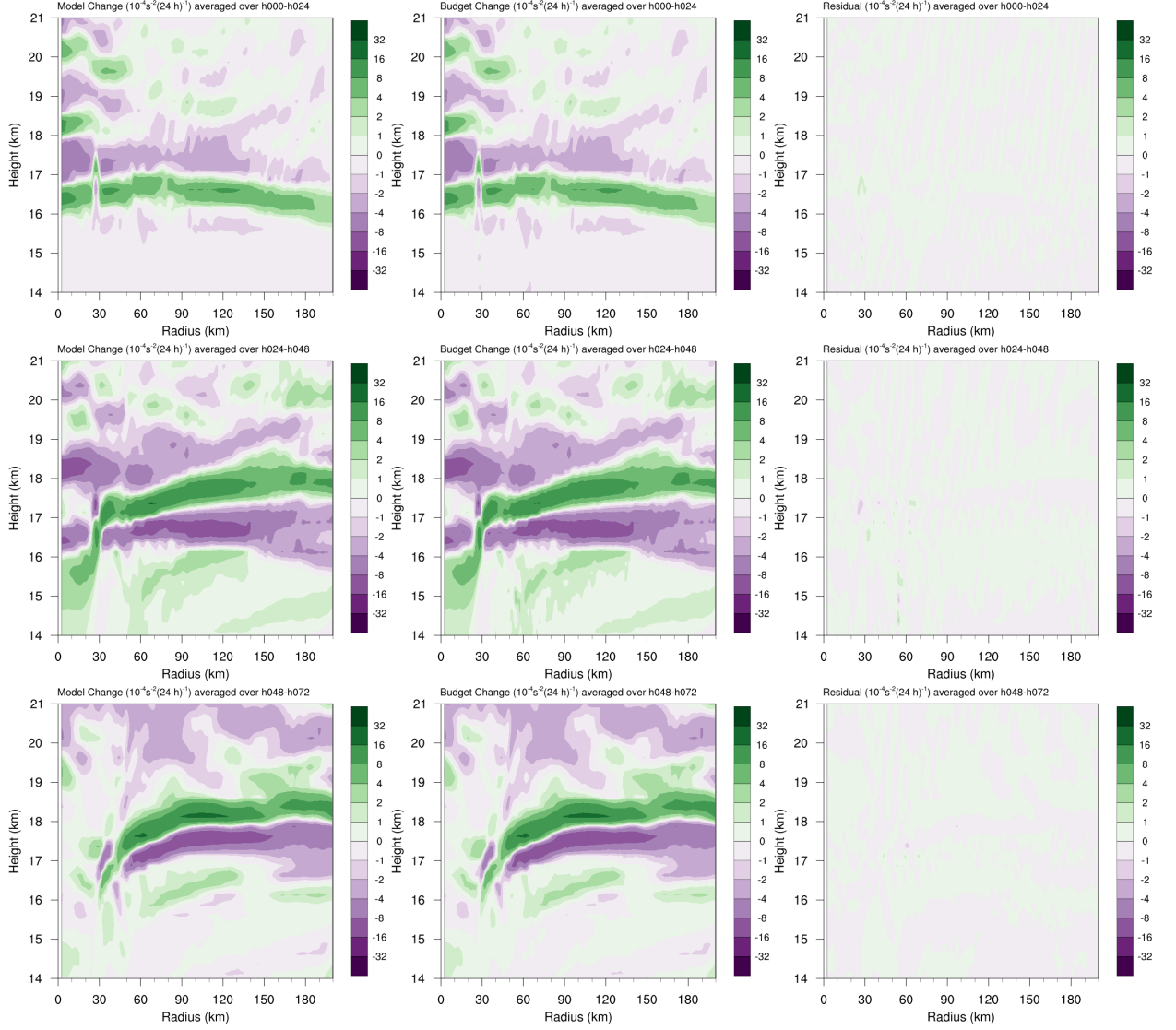
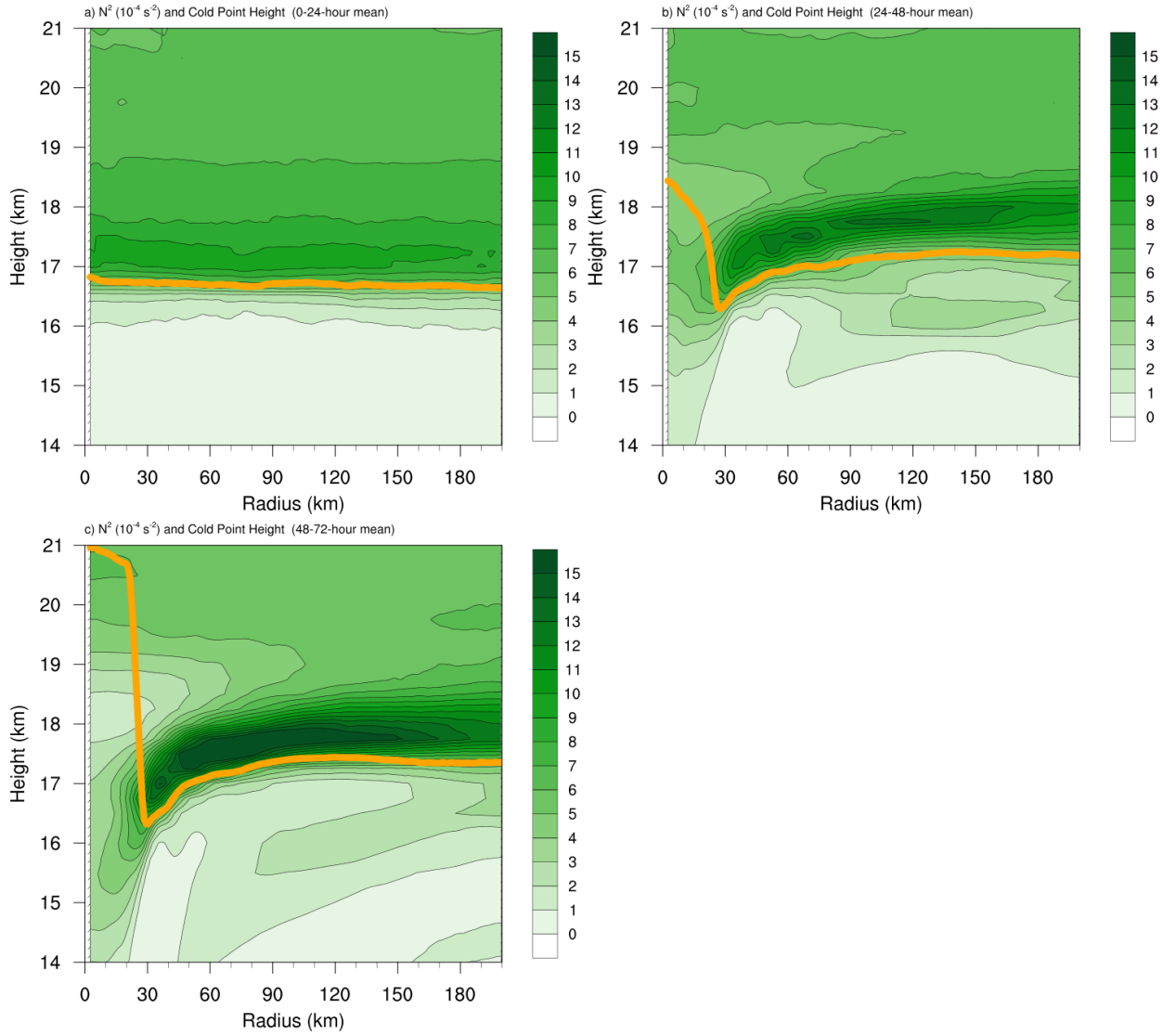


FIG. 2. Left panels: Twenty-four-hour changes in squared Brunt-Väisälä frequency ( $N^2$ ;  $10^{-4} \text{ s}^{-2}$ ) over (top row) 0-24 hours, (middle row) 24-48 hours, (bottom row) 48-72 hours. Middle Panels: The  $N^2$  change over the same time periods computed using Eqs. 4-6, Right Panels: The budget residual over the same time periods, computed by subtracting the budget change (middle column) from the model change (left column).



471 FIG. 3. Twenty-four-hour averages of squared Brunt-Väisälä frequency ( $N^2$ ;  $10^{-4} \text{ s}^{-2}$ ) over (a) 0-24 hours,  
 472 (b) 24-48 hours, (c) 48-72 hours. Orange lines represent the cold-point tropopause averaged over the same time  
 473 periods.

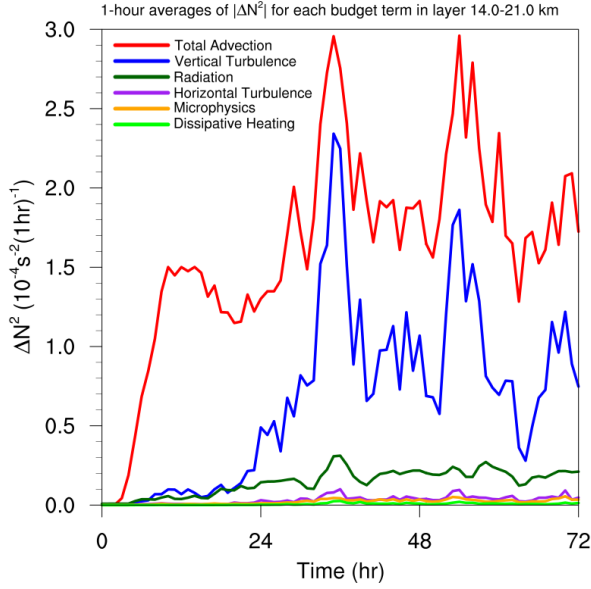
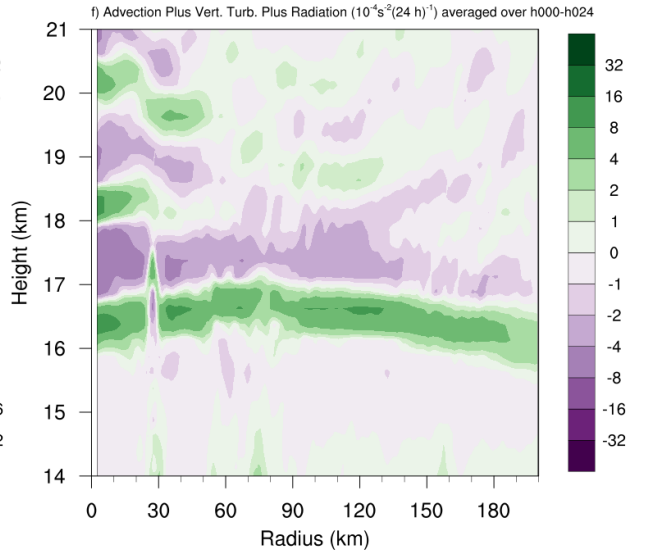
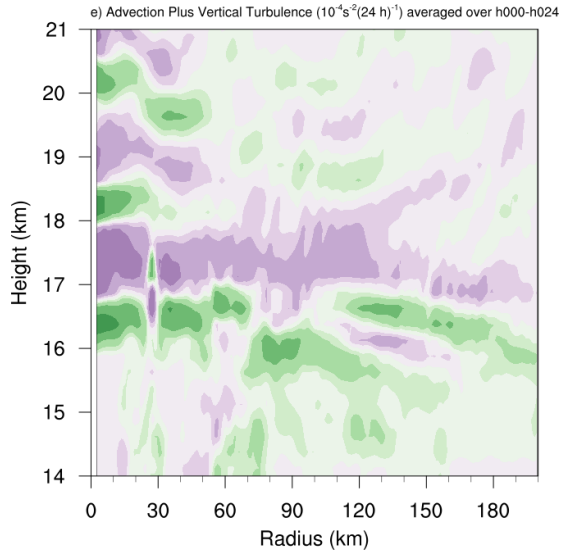
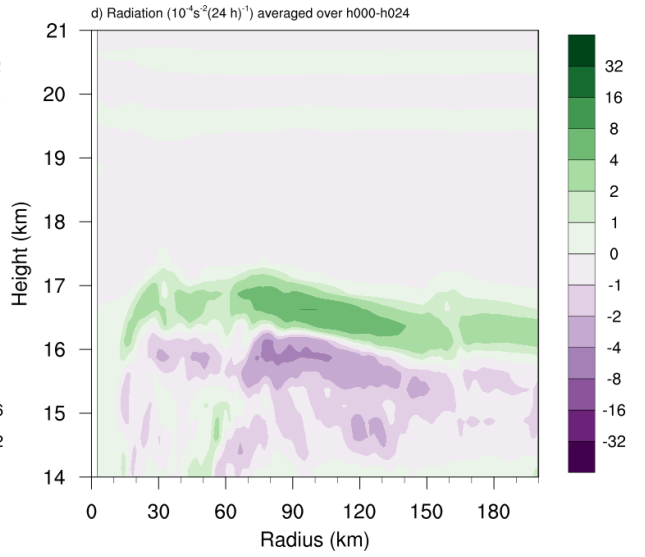
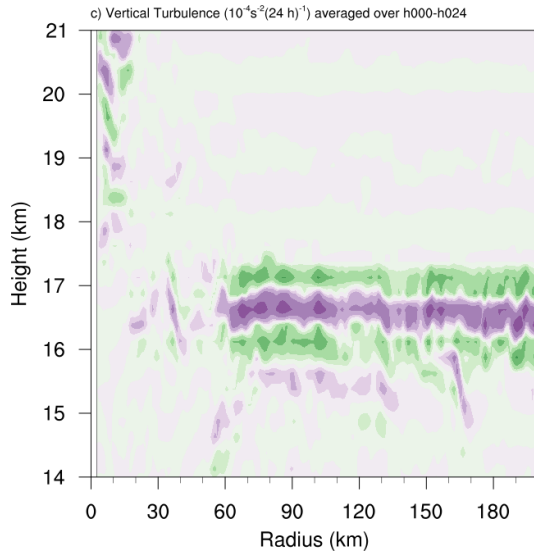
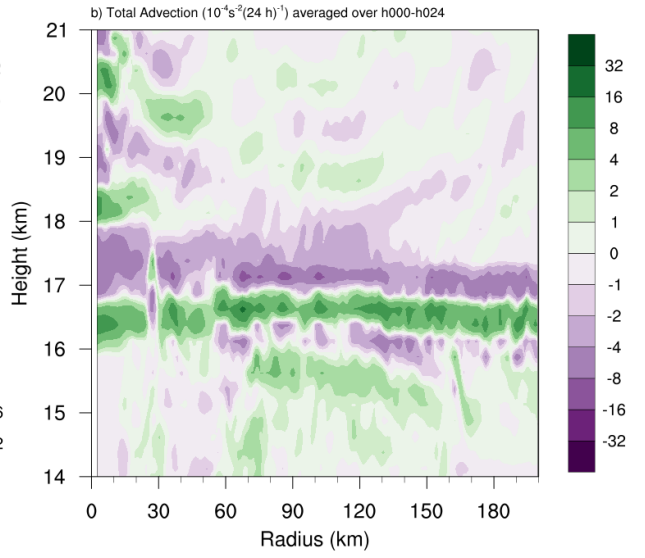
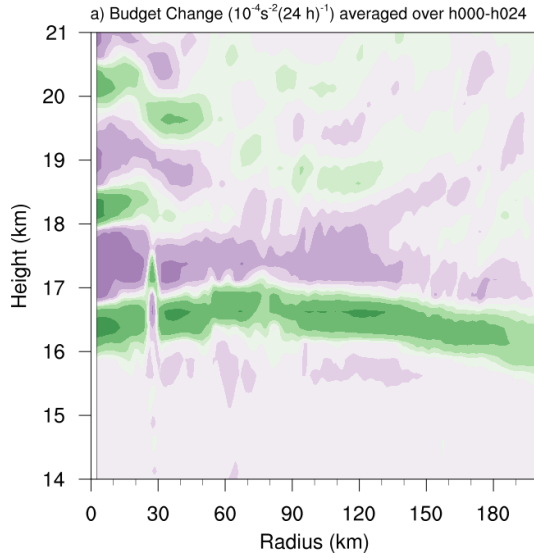


FIG. 4. Time series of the contribution of each of the budget terms to the time tendency of the squared Brunt-Väisälä frequency ( $N^2$ ;  $10^{-4} \text{ s}^{-2}$ ). For each budget term, the absolute value of the  $N^2$  tendency is averaged temporally over 1-hour periods (using output every minute), and spatially in a region extending from 0 to 200 km radius and 14 to 21 km altitude.



478 FIG. 5. (a) Total change in  $N^2$  over the 0-24-hour period ( $10^{-4} \text{ s}^{-2} (24 \text{ h})^{-1}$ ) and the contributions to that change  
479 from (b) the sum of horizontal and vertical advection, (c) vertical turbulence, (d) longwave and shortwave  
480 radiation, (e) the sum of horizontal advection, vertical advection, and vertical turbulence, and (f) the sum of  
481 horizontal advection, vertical advection, vertical turbulence, and longwave and shortwave radiation.

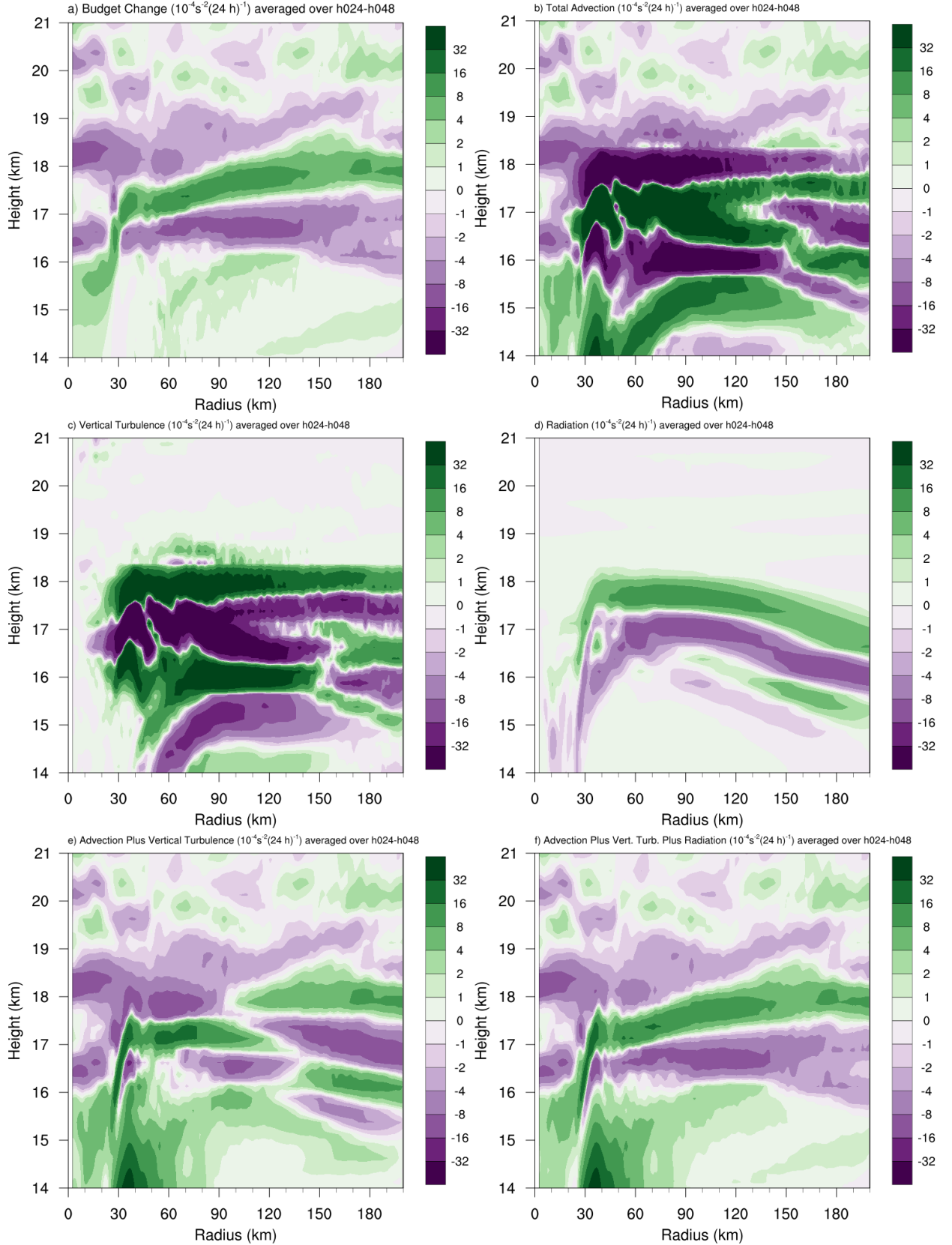


FIG. 6. As in Fig. 5, but for the 24-48-hour period.

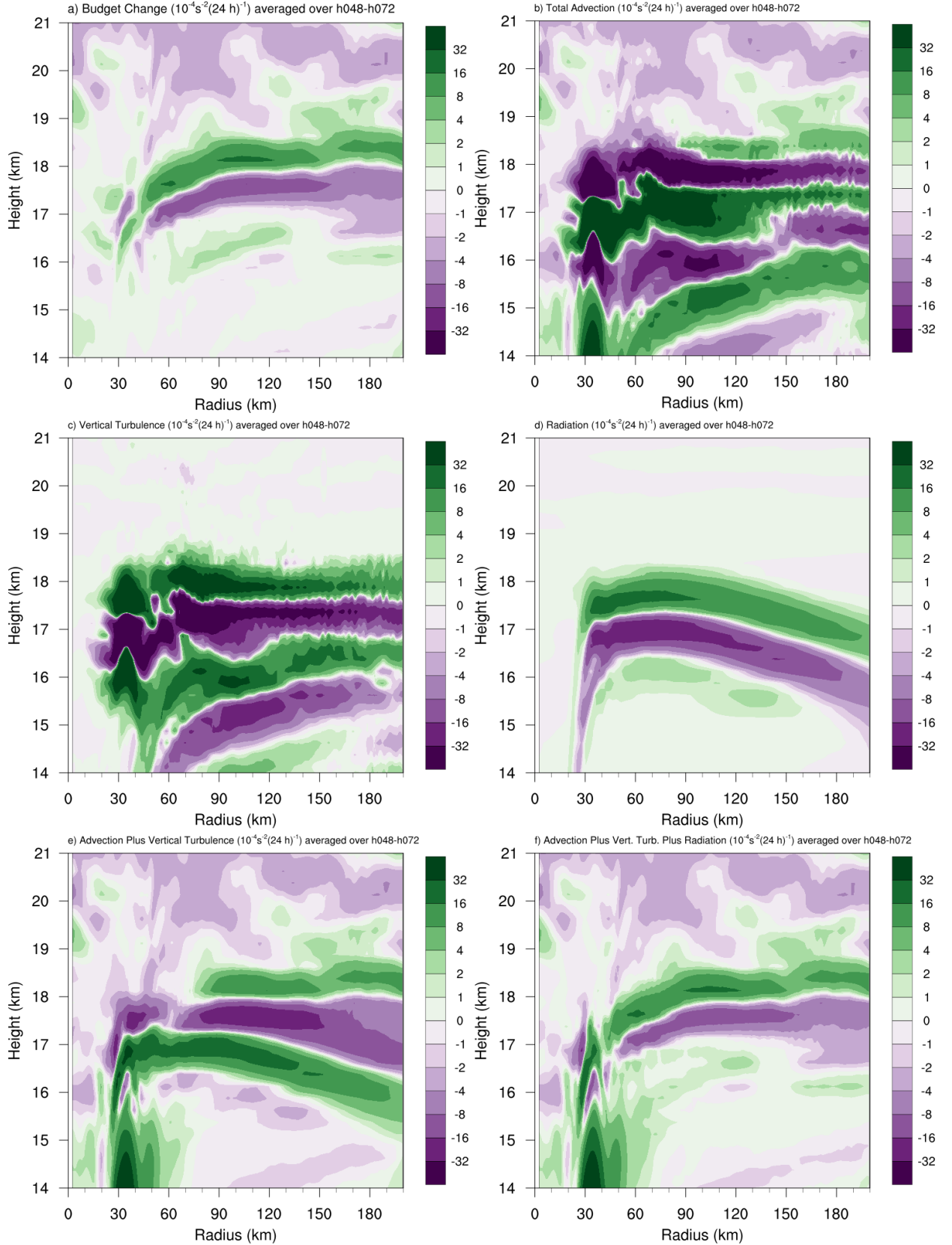


FIG. 7. As in Fig. 5, but for the 48-72-hour period.



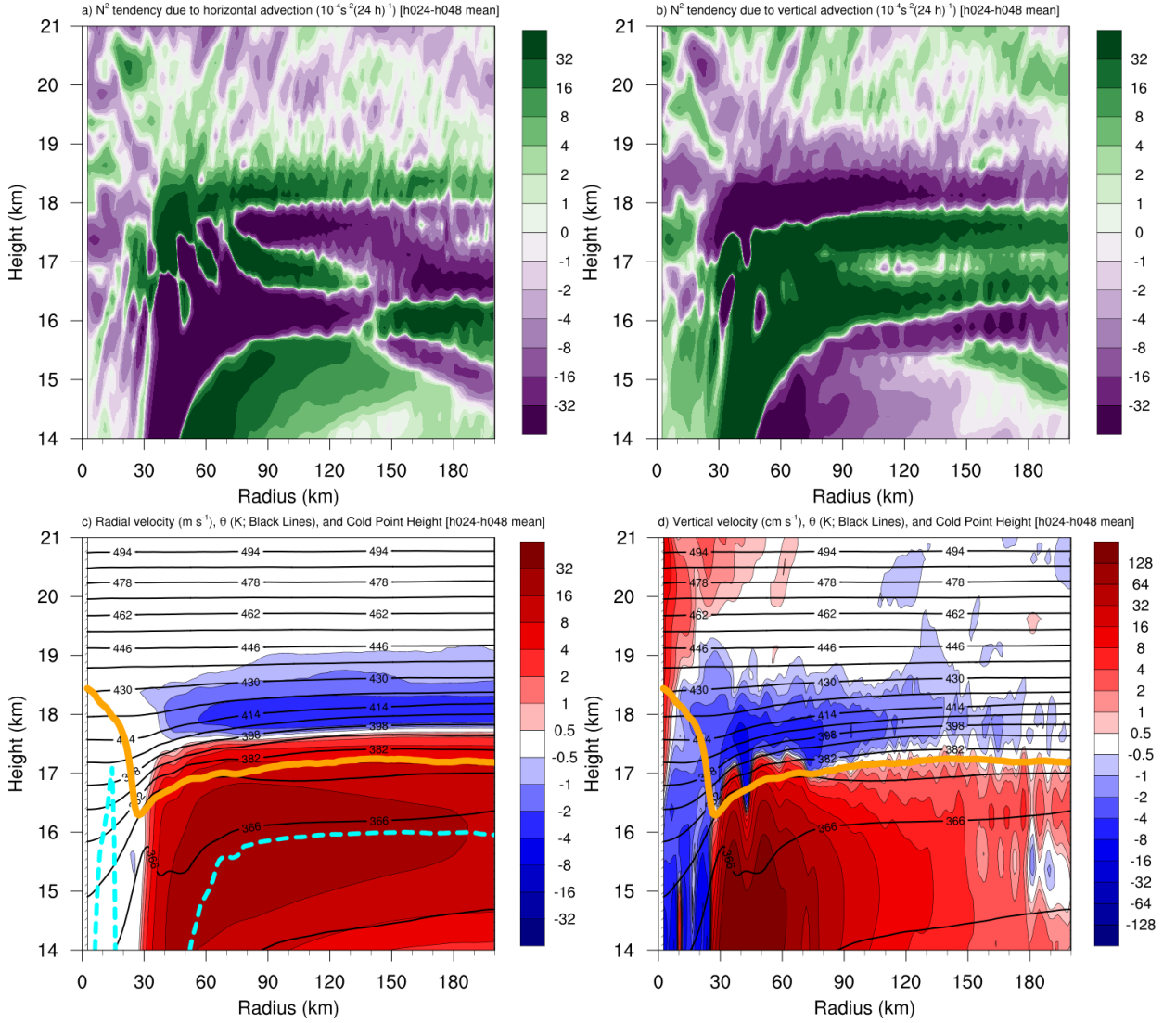
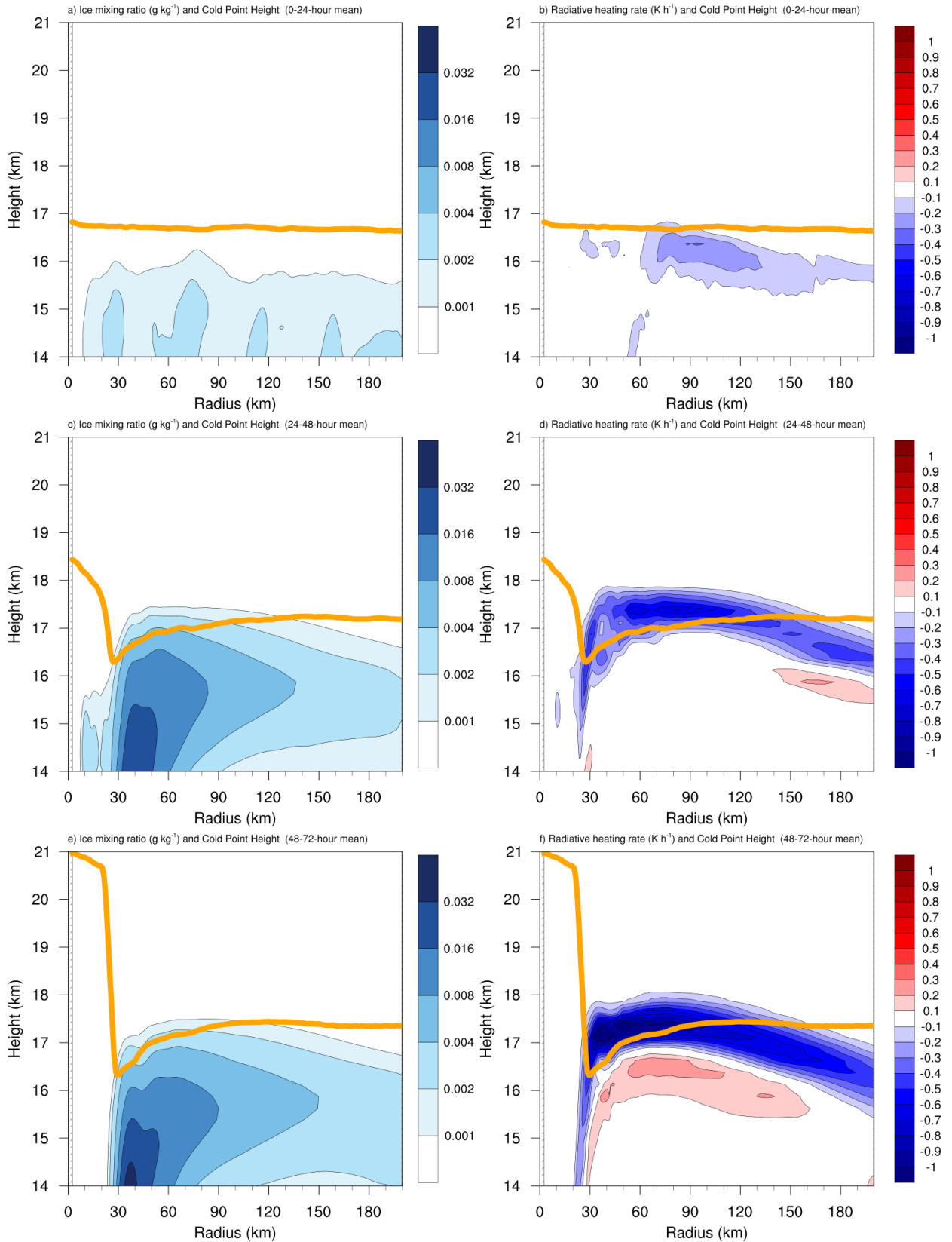


FIG. 8. The contribution to the change in  $N^2$  over the 24-48-hour period ( $10^{-4} \text{ s}^{-2} (24 \text{ h})^{-1}$ ) by (a) horizontal advection and (b) vertical advection. (c) The radial velocity ( $\text{m s}^{-1}$ ; filled contours), potential temperature (K; thick black contours), cold-point tropopause height (orange line), and level of maximum outflow (dashed cyan line) averaged over the 24-48-hour period. (d) The vertical velocity ( $\text{cm s}^{-1}$ ; filled contours), potential temperature (K; thick black contours), and cold-point tropopause height (orange line) averaged over the 24-48-hour period.



488 FIG. 9. Ice mixing ratio ( $\text{g kg}^{-1}$ ) and cold-point tropopause height (orange lines) averaged over (a) 0-24 hours,  
489 (c) 24-48 hours, and (e) 48-72 hours. Radiative heating rate ( $\text{K h}^{-1}$ ) and cold-point tropopause height (orange  
490 lines) averaged over (b) 0-24 hours, (d) 24-48 hours, and (f) 48-72 hours.

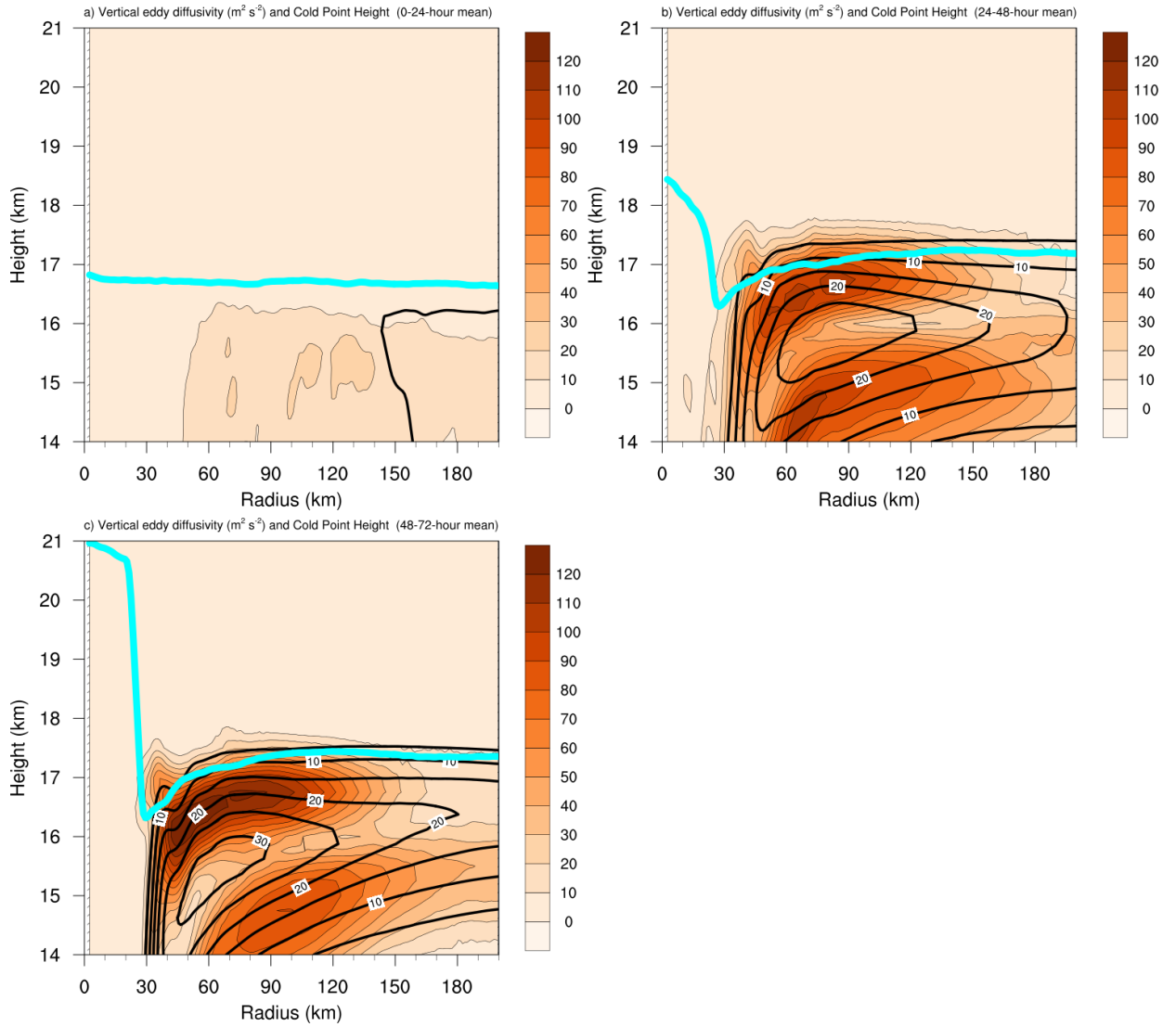


FIG. 10. Vertical eddy diffusivity ( $\text{m}^2 \text{s}^{-2}$ ; filled contours), cold-point tropopause height (cyan lines), and radial velocity ( $\text{m s}^{-1}$ ; thick black lines) averaged over (a) 0-24 hours, (b) 24-48 hours, and (c) 48-72 hours.

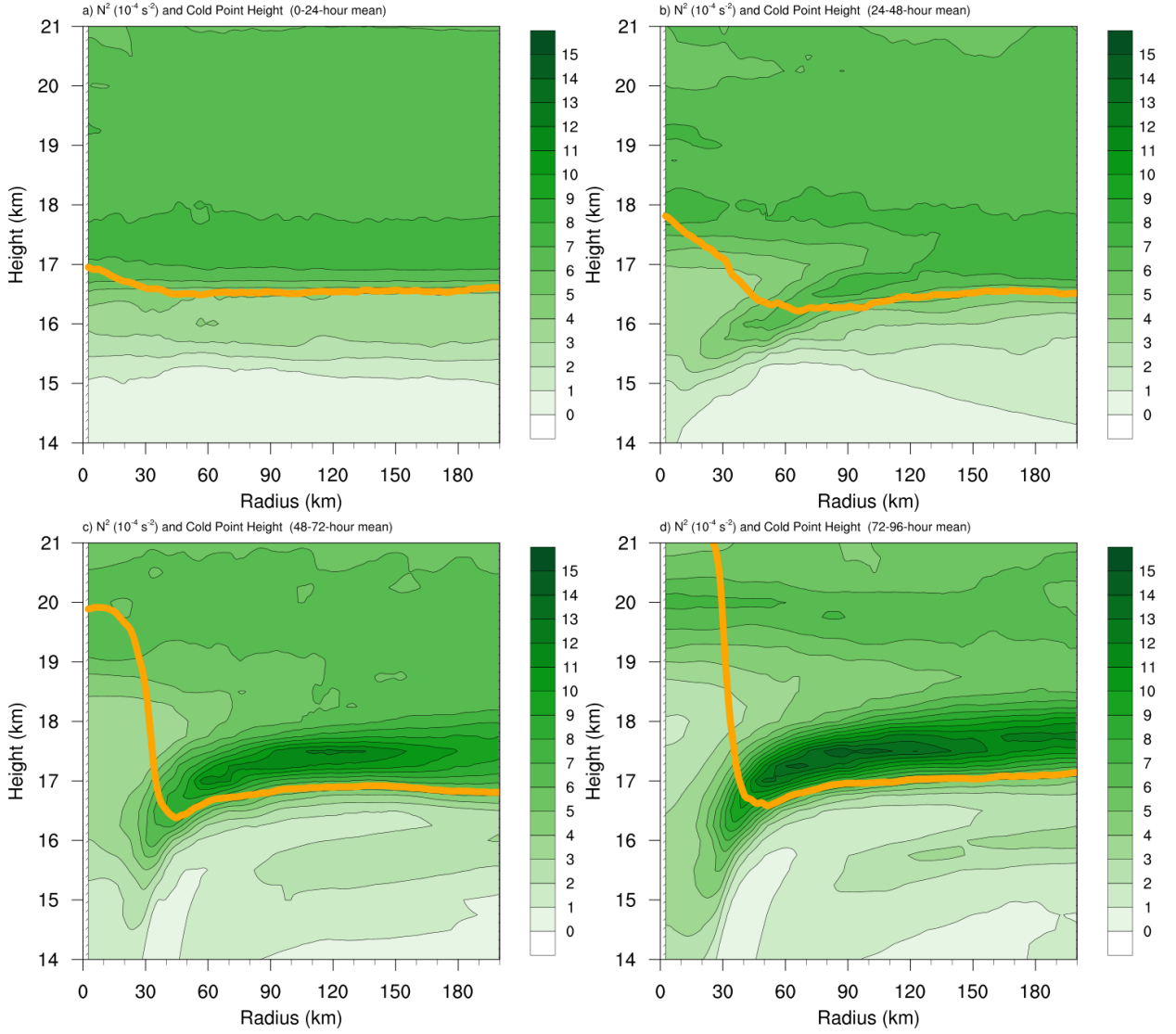
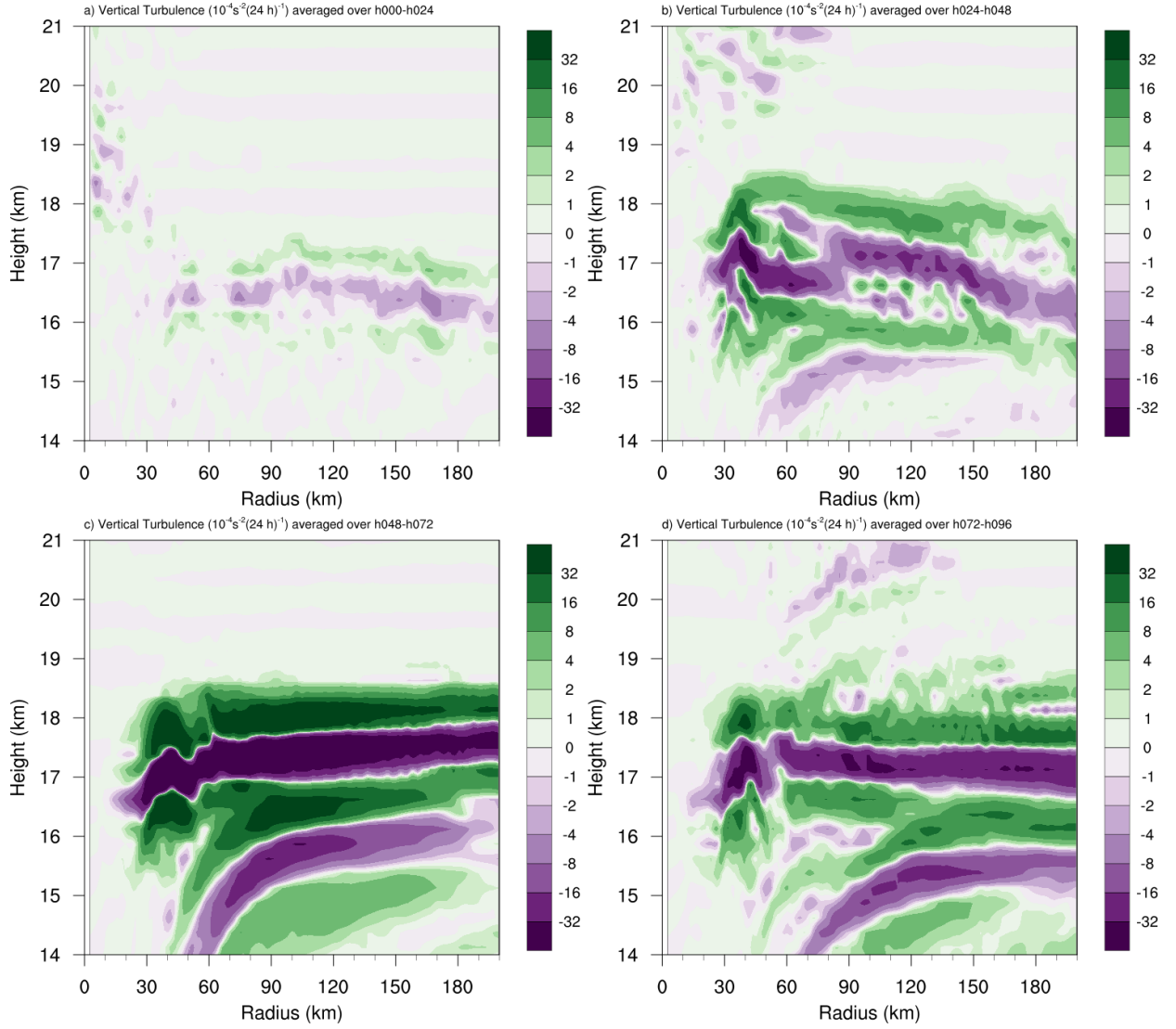


Fig. A1. Twenty-four-hour averages of squared Brunt-Väisälä frequency ( $N^2$ ;  $10^{-4} \text{ s}^{-2}$ ) over (a) 0-24 hours, (b) 24-48 hours, (c) 48-72 hours, and (d) 72-96 hours for the simulation described in Appendix Aa. Orange lines represent the cold-point tropopause averaged over the same time periods.



496 Fig. A2. The contribution of vertical turbulence to the  $N^2$  variability ( $10^{-4} \text{s}^{-2} (24 \text{ h})^{-1}$ ) averaged over (a) 0-24  
 497 hours, (b) 24-48 hours, (c) 48-72 hours, and (d) 72-96 hours for the simulation described in Appendix Ab.